



# Efficiency Enhancement by BSF Optimization on Cu (In<sub>1-x</sub> Ga<sub>x</sub>) Se<sub>2</sub> Solar Cells with Tin (IV) Sulfide Buffer Layer

Zineb Benbouzid<sup>1</sup> · Wafà Benstaali<sup>2,3</sup> · Wassila Leila Rahal<sup>4,5</sup> · Nouredine Hassini<sup>1,5</sup> · Mohammed Ridha Benzidane<sup>1</sup> · Abdelkader Boukortt<sup>1,3</sup>

Received: 1 March 2023 / Accepted: 24 March 2023 / Published online: 18 April 2023  
© The Minerals, Metals & Materials Society 2023

## Abstract

This paper aims to investigate the photovoltaic performance of copper indium gallium selenide (CIGS) solar cells using SCAPS-1D (Solar Cell Capacitance Simulator in One Dimension) software. The novelty in this research revolves around applying lamellar tin sulfide (SnS<sub>2</sub>) as a buffer layer and tin monosulfide (SnS) as a back surface field (BSF) layer, which is noteworthy since few materials have previously been exploited in CIGS solar cell research. The studied solar cell is composed of four layers with different physical parameters: two *p*-type doped layers, SnS as the BSF layer and the CIGS as the absorption layer, as well as two other *n*-type doped layers, SnS<sub>2</sub> as the buffer layer and aluminium-doped zinc oxide (AZO) as the window layer. This work covered the role and effect of the BSF (SnS) layer on the photovoltaic parameters of the CIGS solar cell device. In addition, the variation of thickness, acceptor concentration, band gap and operating temperature of the SnS layer was also optimized and analysed. Adding the BSF (SnS) layer between the absorber layer (CIGS) and the metal back contact (molybdenum [Mo]) leads to increased hole tunnelling activity, resulting in a quasi-ohmic contact of the Schottky type near the back surface. Thus, this contact improves the electric field region generated at the back interface. Also, reducing back surface recombination increases energy conversion efficiency. As a result, the inclusion of a 40 nm thin film of BSF layer at the optimum temperature of 300 K significantly enhanced the device's open-circuit voltage ( $V_{OC}$ ) from 0.73 V to 0.87 V, current density ( $J_{SC}$ ) from 36 mA/cm<sup>2</sup> to 40 mA/cm<sup>2</sup>, fill factor (FF) from 84% to 86%, and power conversion efficiency (PCE) from about of 22% to 30%, for an absorption layer thickness of 1 μm. These findings offer great promise for the efficiency and economic viability of CIGS solar cells in the future.

**Keywords** Solar cells · CIGS · buffer layer · SnS · SnS<sub>2</sub> · BSF · efficiency · SCAPS-1D

## Introduction

A thin-film solar cell (TFSC) is a highly efficient, cost-effective, and long-lasting device for meeting the world's demand for renewable energy in the photovoltaic (PV) sector. Recently, researchers have been more interested

in non-silicon semiconductor materials such as cadmium telluride (CdTe) and copper indium gallium selenide (CIGS) due to their high photo-conversion efficiency and suitability for large-scale commercial manufacturing in PV systems technology.<sup>1–4</sup> The global research community is increasingly interested in polycrystalline CIGS-based

✉ Zineb Benbouzid  
zineb.benbouzid.etu@univ-mosta.dz

<sup>1</sup> Elaboration and Characterization Physico-Mechanical and Metallurgical of Materials Laboratory (ECP3M), Abdelhamid Ibn Badis University-Mostaganem, Route Nationale N°11, Kharrouba, 27000 Mostaganem, Algeria

<sup>2</sup> LPPMCA Laboratory of Plasma Physics, Conductive Materials and Their Applications, University of Science and Technology of Oran Mohamed Boudiaf, 31000 Oran, Algeria

<sup>3</sup> Faculty of Sciences and Technology, Abdelhamid Ibn Badis University, Route de Belhacel, B. P. 227, 27000 Mostaganem, Algeria

<sup>4</sup> Laboratory of Analysis and Application of Radiation, Faculty of Physics, University of Sciences and Technology of Oran Mohamed Boudiaf, USTO-MB, BP 1505, Oran, Algeria

<sup>5</sup> Physics Department, Faculty of Exact Sciences and Computer Science, University Abdelhamid Ibn Badis of Mostaganem, Chemin des Crêtes, 27000 Mostaganem, Algeria

materials to manufacture low-cost, high-efficiency solar cells. In a typical CIGS cell, an active layer of CIGS serves as the main light absorber layer, which absorbs the majority of incident photons on the device. To create a  $p$ - $n$  junction with the absorber layer, an  $n$ -type cadmium sulfide (CdS) buffer layer, is placed between the  $p$ -type CIGS active layer and the window layer. A transparent conductance oxide (TCO) acting as a window layer AZO is interfaced with a CdS layer to collect electrons on the front side. The window layer decreases surface defect density considerably, resulting in a drop in surface recombination velocity.<sup>5</sup>

At present, the overall efficiency of CIGS-based PV cells using conventional CdS buffer is 23.35%<sup>6–8</sup> at the laboratory scales. In contrast, the main downside of CdS buffer is its toxicity, which causes environmental and human health problems.<sup>9,10</sup> Until now, considerable effort has been expended to replace it with a variety of alternative buffer layers, such as zinc sulfide (ZnS)<sup>11,12</sup> zinc selenide (ZnSe),<sup>13,14</sup> indium(III) sulfide (In<sub>2</sub>S<sub>3</sub>).<sup>1,14</sup> Furthermore, tin sulfide (SnS<sub>2</sub>) is a simple binary IV–VI group metal chalcogenide that is safe and inexpensive.<sup>15</sup> As a result, SnS<sub>2</sub> has good potential as a non-toxic buffer layer in solar cells.<sup>16–19</sup> A variety of new semiconductors have been proposed in recent years to produce enhanced and more efficient solar cells, including organic materials, II–VI compounds and perovskites. One of the more promising materials, without a doubt, is CIGS, which performs very well in terms of lifetime and processability while maintaining high conversion efficiency.<sup>20</sup> Copper indium selenide (CIS) and copper gallium selenide (CGS) are ternary compounds of a Cu (In<sub>1-x</sub>, Ga<sub>x</sub>) Se<sub>2</sub> solid solution, belonging to quaternary elements I, III, and VI of the periodic table.<sup>5,21</sup> Chalcopyrite CIGS is thought to be a promising option for future thin-film (PV) technologies due to its high absorption coefficient of approximately  $10^7 \text{ m}^{-1}$ ,<sup>22</sup> and good spectral response over a wide range of wavelengths in the solar spectrum.<sup>23</sup> As is known, the performance of a PV cell is determined by three elements which are charge generation, exciton dissociation, and collection of the generated charge carrier, but the back surface recombination and semiconductor (CIGS)/metal (Mo) contact interface recombination reduce solar cell efficiency.<sup>24</sup> A suitable back contact metal with a high work function is necessary to improve cell efficiency. Because most metals lack sufficient work functions, a Schottky-barrier contact is created between the metal electrode Mo and the CIGS layer interface. This Schottky barrier can significantly impact the current–voltage ( $I$ – $V$ ) characteristics of a CIGS solar cell, principally by limiting hole transport. Hence a better metal with high work function is required to create an ohmic contact with CIGS active layer. To overcome this barrier, a known strategy is to

either minimize the barrier height or moderate its breadth by strongly doping an additional layer of the back surface field (BSF) with appropriate material between the active layer and the metal back contact.<sup>22</sup>

One of the main culprits responsible for the relatively low efficiency of CIGS solar cells is the back surface recombination, which limits the carrier collection efficiency and reduces the device's overall performance. It has been shown that the BSF can play a crucial role in reducing the back surface recombination where it creates a rear pushing force at the extensively doped backside of the structure to push the minority carrier to the depletion area, thereby passivating the back surface and reducing rear recombination of the solar device, which leads to the improvement of the electrical properties, where the cost of device manufacture can be decreased due to this phenomenon by lowering the thickness of the absorber layer and improving the efficiency of the solar cell.<sup>5,21</sup> In this work, the proposed thin-layer solar cell structure using tin monosulfide (SnS) and SnS<sub>2</sub> as BSF and buffer layers is a novel approach that can potentially address the back surface recombination issue and improve the device's overall performance. We chose SnS and SnS<sub>2</sub> based on their electronic properties and compatibility with CIGS. The band gap and band alignment of SnS and SnS<sub>2</sub> are well suited for use as a buffer and BSF layers in CIGS solar cells. The proposed structure has the potential to significantly improve the efficiency and stability of CIGS solar cells by reducing the back surface recombination and increasing the carrier collection efficiency. This can lead to a reduction in the cost per watt of solar energy and make it more competitive with other forms of energy.

Furthermore, using SnS and SnS<sub>2</sub> as BSF and buffer layers is an attractive option due to their low toxicity and low-cost fabrication process. This can help address the environmental concerns associated with producing and disposing of solar cells. Despite the promising performance of CIGS solar cells, there is still a need for further research to improve their efficiency and stability.

In this study, we evaluate the performance of CIGS solar cells using SCAPS-1D (Solar Cell Capacitance Simulator in One Dimension, version 3.3.07). The main goal is to insert a BSF (SnS) or BSF-P<sup>+</sup> using a SnS<sub>2</sub> buffer layer in CIGS photovoltaic cells. A BSF layer consists of a higher doped region at the rear face of the solar cell CIGS. The interface between the high and low-doped regions behaves like a  $p$ - $n$  junction, forming an electric field at the interface, which introduces a barrier to minority carrier flow to the rear surface. The new structure that we proposed (Mo/SnS/CIGS/SnS<sub>2</sub>/AZO) was numerically analysed to obtain the solar cell performance parameters; open-circuit voltage ( $V_{OC}$ ), short-circuit current density ( $J_{SC}$ ), fill factor (FF), and power conversion efficiency (PCE).

## Physical Parameters and Modelling

### Equations and Simulation Methods

The simulation modelling of our CIGS-based solar cell structure has been carried out using SCAPS (Solar Cell Capacitance Simulator), which is a one-dimensional solar cell simulation program developed at the Department of Electronics and Information Systems (ELIS) of the University of Ghent, Belgium,<sup>24</sup> that is used for numerical simulation of thin-film solar cells (TFSCs). The SCAPS 1-D program solves the equations for structures containing a certain number of semiconductor layers with an arbitrary doping profile (as a function of position) with an arbitrary energy distribution of the deep donor or acceptor levels under different types of illumination.

The study of semiconductor devices is based on the simultaneous resolution of the Poisson equation (Eq. 1), the continuity equation for electrons (2) and for holes (3) with the appropriate limit conditions.

$$\frac{d^2}{dx^2} \Psi(x) = \frac{e}{\epsilon_0 \epsilon_r} (p(x) - n(x) + N_D - N_A + \rho_p - \rho_n) \quad (1)$$

$$\frac{d}{dx} J_n(x) - e \frac{\partial n(x)}{\partial t} - e \frac{\partial \rho_n}{\partial t} = G(x) - R(x) \quad (2)$$

$$\frac{d}{dx} J_p(x) + e \frac{\partial p(x)}{\partial t} + e \frac{\partial \rho_p}{\partial t} = G(x) - R(x) \quad (3)$$

In these equations,  $\psi$  indicates the electrostatic potential,  $\epsilon_0$  the vacuum and  $\epsilon_r$  the relative permittivity of the static material,  $e$  represents the elementary charge ( $1.6 \times 10^{-19}C$ ),  $n$  and  $p$  represent the density of electrons and holes, respectively,  $N_A$  and  $N_D$  correspond to the densities of ionized acceptors and donors.  $\rho_p/\rho_n$  depict the hole and electron distribution,  $J_p/J_n$  is the hole and the electron current density, and  $G(x)$  and  $R(x)$  are the charge generation and the recombination rates, respectively.

Equations 4 and 5 can be used to analytically depict the performance fill factor (FF) and power conversion (PCE) of photovoltaic systems.

$$FF = \frac{P_{max}}{P_{th}} = \frac{V_{max} \times J_{max}}{V_{OC} \times J_{SC}} \quad (4)$$

$$PCE = \frac{V_{OC} \times J_{SC} \times FF}{P_{th}} \quad (5)$$

### Device Structure and Material Parameters

The suggested solar device's structure in this research is coated on soda-lime glass (SLG). The first layer of Mo

is used as a back contact. The second layer is the CIGS, which is an active layer that acts as an absorption layer. A highly SnS-P + doped layer (BSF) is placed between the p-CIGS semiconductor and the back contact metal (Mo). The  $n$ -type semiconductor material SnS<sub>2</sub> is suggested as a buffer layer that is a reasonable substitute for CdS due to the toxicity of Cd, followed by Al-doped ZnO (AZO) as a window layer. Finally, aluminium (Al) serves as the front contact of the device. The investigated solar cell structure SLG/Mo/SnS/CIGS/SnS<sub>2</sub>/AZO/Al is illustrated in Fig. 1. The following scientific references<sup>5,23,26-34</sup> include the input's physical parameters that are used in the numerical simulation, which are illustrated in Table I.

The quantity of current flowing through the solar device SnS/CIGS/SnS<sub>2</sub>/AZO is ascertained by the band gap alignment presented in Fig. 2. A Schottky barrier is created between both the absorber layer and the Mo contact, which has a metal work function of  $\Phi_m = 5 \text{ eV}$ <sup>24</sup> less than  $E_g + \chi$  ( $E_g + \chi > \Phi_m$ ),<sup>22,29</sup> where  $E_g$  is the band gap and  $\chi$  indicates the electron affinity. Generally, the electron is captured when it reaches the back surface Mo and is not able to contribute to the current, while the BSF layer between CIGS and Mo can decrease the barrier height by creating a quasi-ohmic contact and allowing the electron to reach the buffer layer and contribute to the photovoltaic effect again. The SnS layer provides the supplementary holes tunnelling to shape the quasi-ohmic contact and lower the recombination rate of the back surface.

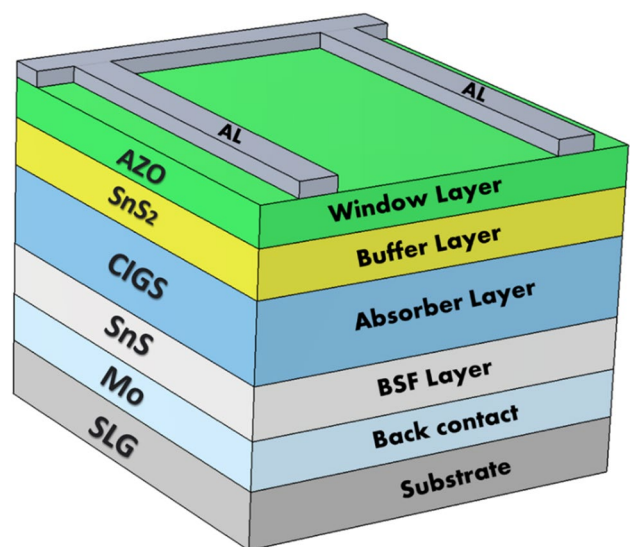
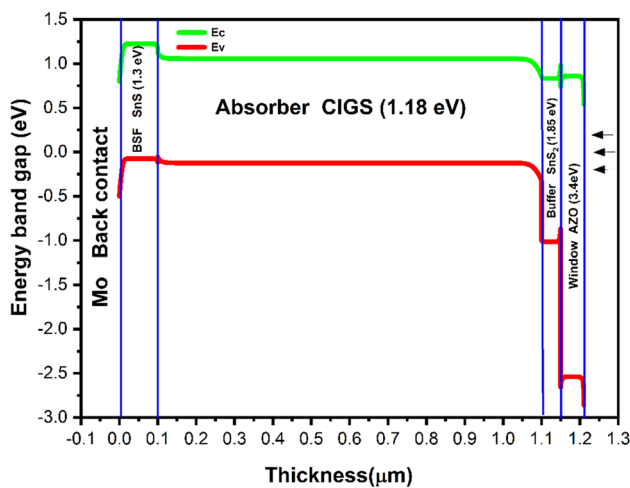


Fig. 1 Schematic diagram of the suggested CIGS-based solar device.

**Table 1** SCAPS input parameters for the initial device configuration at 300 K.

Material properties	Units	CIGS ( <i>p</i> )	SnS <sub>2</sub> ( <i>n</i> )	AZO ( <i>n</i> )	SnS ( <i>p</i> <sup>+</sup> )
Thickness	μm	1 <sup>25</sup>	0.05 <sup>27</sup>	0.06 <sup>29</sup>	0.01–0.1
$E_g$	eV	1.18 <sup>5</sup>	1.85 <sup>27</sup>	3.4 <sup>30</sup>	1.3 <sup>33</sup>
Electron affinity, $\chi$	eV	4.26 <sup>5</sup>	4.26 <sup>27</sup>	4.5 <sup>23</sup>	4.2 <sup>33</sup>
Relative dielectric permittivity, $\epsilon$	–	13.6 <sup>25</sup>	17.7 <sup>27</sup>	9 <sup>31</sup>	12.5 <sup>33</sup>
CB effective density of states, $N_c$	cm <sup>-3</sup>	$2.2 \times 10^{1825}$	$7.32 \times 10^{1827}$	$2.2 \times 10^{1831}$	$1 \times 10^{1933}$
VB effective density of states, $N_v$	cm <sup>-3</sup>	$1.8 \times 10^{1925}$	$1.8 \times 10^{1927}$	$1.8 \times 10^{1931}$	$4.13 \times 10^{1933}$
Thermal velocities, $V_{thn}$ , $V_{thp}$	cm/s	$1 \times 10^{725}$	$1 \times 10^{727}$	$1 \times 10^{731}$	$1 \times 10^{733}$
Electron mobility, $\mu_n$	cm <sup>2</sup> /Vs	100 <sup>25</sup>	50 <sup>27</sup>	100 <sup>31</sup>	25 <sup>33</sup>
Hole mobility, $\mu_p$	cm <sup>2</sup> /Vs	25 <sup>25</sup>	25 <sup>27</sup>	25 <sup>31</sup>	10 <sup>33</sup>
Donor density, $N_D$	cm <sup>-3</sup>	0	$9.85 \times 10^{1827}$	$1 \times 10^{1831}$	0
Acceptor density, $N_A$	cm <sup>-3</sup>	$2 \times 10^{1726}$	0	0	$3 \times 10^{1833}$
Defect density, $N_t$	cm <sup>-3</sup>	$1 \times 10^{1425}$	$1 \times 10^{1628}$	$3 \times 10^{1632}$	$1 \times 10^{1434}$

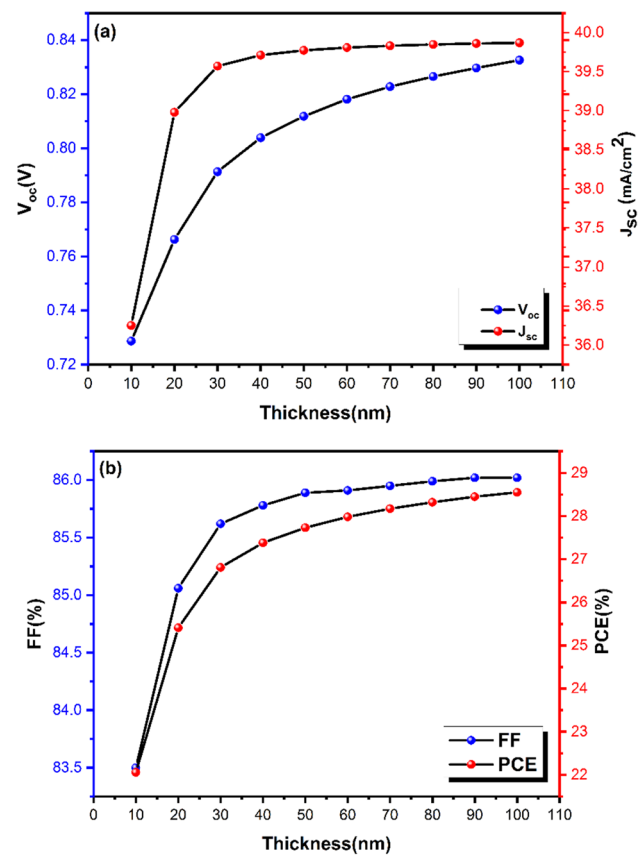
**Fig. 2** Band diagram structure of the studied CIGS solar cell with BSF.

## Results and Discussion

We have theoretically investigated a CIGS thin-film solar cell with SnS<sub>2</sub> emitter layer and SnS BSF layer under AM 1.5G illumination at a temperature of 300 K, where we have changed the BSF layer thickness, acceptor densities, and band gap to examine the performance of the solar cell, keeping all other parameters unchanged.

### Effect of BSF (SnS) Layer Thickness on CIGS Cell Performance

In this optimization research, the effect of BSF SnS layer thickness on the performance of photovoltaic CIGS cells was investigated by varying the thickness of the SnS layer from 10 nm to 100 nm, at the same time keeping

**Fig. 3** The effect of BSF (SnS) layer thickness on solar device performance. (a) Variation of  $V_{oc}$  and  $J_{sc}$ . (b) Variation of FF and PCE.

the thickness of the CIGS layer constant (1 μm) and  $N_A$  (SnS) =  $3 \times 10^{18}$  cm<sup>-3</sup>. The resulting findings of  $V_{oc}$ ,  $J_{sc}$ , FF, and PCE are illustrated in Fig. 3. According to the results of the findings, it is noticeable that as the BSF (SnS) thickness increases, the  $V_{oc}$  increases monotonically from 0.73 V to 0.80 V. On the other hand,  $J_{sc}$  (36.25 mA/cm<sup>2</sup> to 39.71 mA/cm<sup>2</sup>) and FF (83.50% to 85.78%)

increase almost linearly when the thickness increases from 10 nm to 40 nm. The PCE nearly follows the FF trend, increasing from 22.06% to 27.38%. The characteristics of current density–voltage ( $J$ – $V$ ) and quantum efficiency (QE) are illustrated in Figs. 4 and 5, respectively. It is found that the thickness of the BSF (SnS) layer has a strong influence on these curves. In Fig. 4,  $V_{OC}$  increases significantly in parallel with SnS- $P^+$  layer thickness and then saturates at thicknesses greater than 40 nm (0.04  $\mu$ m). An electric field is created due to the formation of a  $p$ – $p^+$  junction at the interface between SnS- $P^+$  and  $p$  CIGS which behaves as a potential barrier for electron transport to the back surface. Electron backscattering reduces the dark current while increasing the  $J_{SC}$ .<sup>35</sup> The 40 nm width of the SnS- $P^+$  layer enables a short-circuit current density of 39.7 mA/cm<sup>2</sup> and an energy efficiency of approximately 27.38%. In addition, Fig. 5 shows a rise in the external quantum efficiency. The spectra obtained in the long wavelength region (780–1100 nm) clearly show the extended optical absorption beyond 20 nm thickness. As a result, a BSF layer thickness of 40 nm is appropriate, with a similar impact on cell performance.

#### Effect of BSF (SnS) Layer Acceptor Concentration on CIGS Cell Performance.

BSF has an essential part in the collection of photo-generated carriers in the CIGS active layer. The acceptor density of the BSF (SnS) material increases from  $3 \times 10^{15}$  cm<sup>-3</sup> to  $3 \times 10^{19}$  cm<sup>-3</sup> at 40 nm constant thickness of the SnS- $P^+$

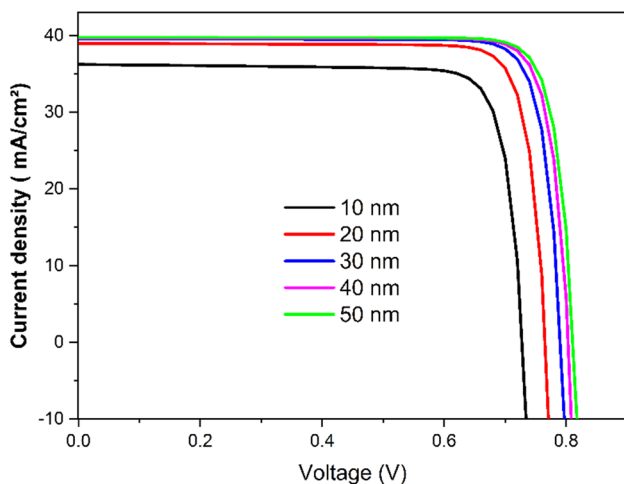


**Fig. 4**  $J$ – $V$  characteristic of CIGS-based solar cells for various thicknesses of BSF (SnS) layer.

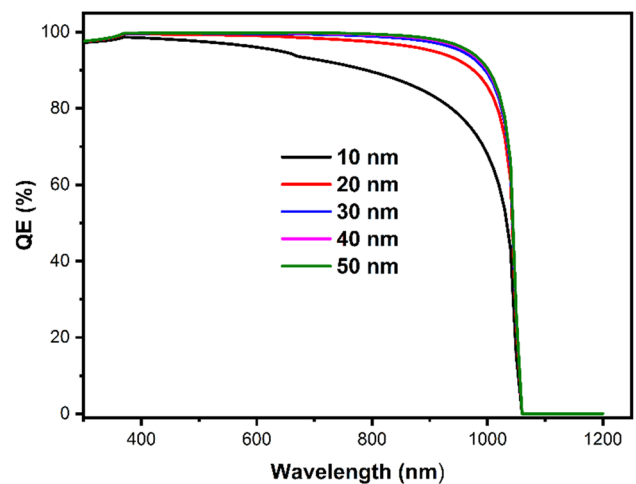


**Fig. 5** Quantum efficiency of CIGS based solar cells for various thicknesses of BSF (SnS) layer.

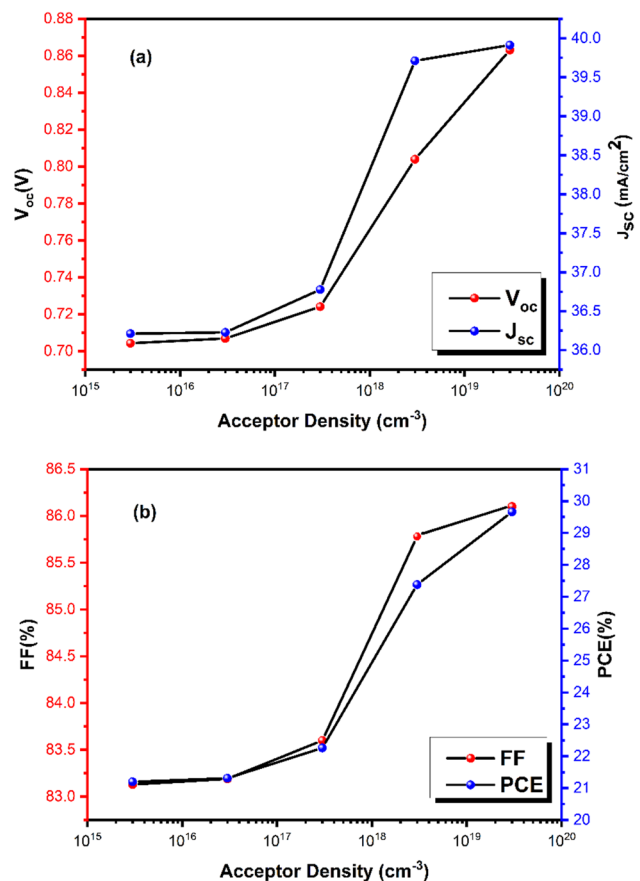


**Fig. 6** The effect of BSF (SnS) acceptor density on solar device performance. (a)  $V_{OC}$  and  $J_{SC}$  variation. (b) FF and PCE variation.

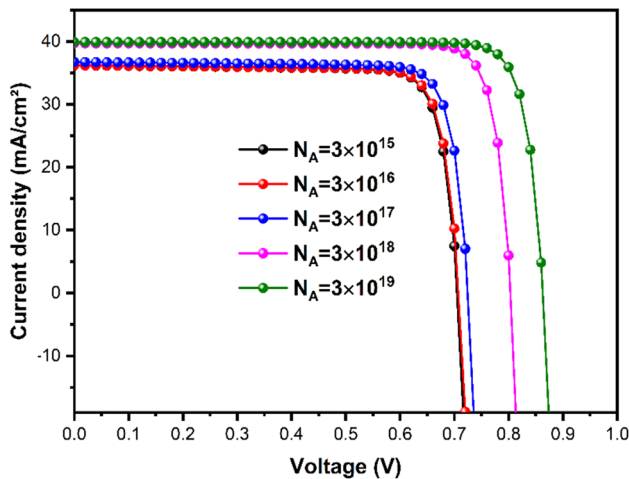


**Fig. 7**  $J$ - $V$  characteristic of CIGS-based solar cells with BSF (SnS) for different acceptor density values.

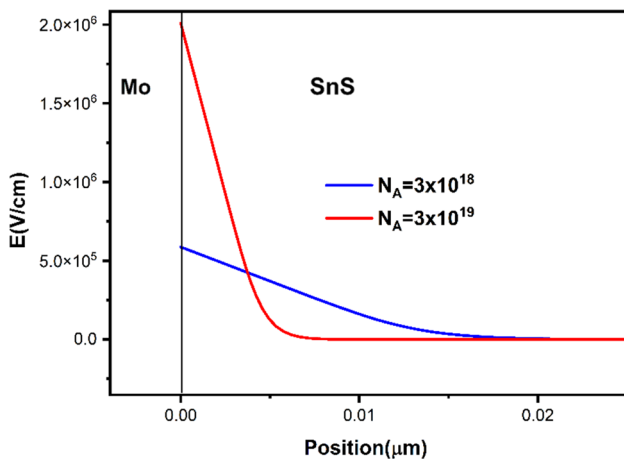


**Fig. 8** Electric field for a CIGS solar cell with two values of acceptor density.

layer, as depicted in Fig. 6. We observe that the short-circuit current density increases from 39.71 mA/cm<sup>2</sup> to 39.91 mA/cm<sup>2</sup>, FF from 85.78% to 86.10%, and PCE from 27.38 to 29.66% when the acceptor doping concentration is increased from  $3 \times 10^{18}$  cm<sup>-3</sup> to  $3 \times 10^{19}$  cm<sup>-3</sup>. The  $J$ - $V$  curve is illustrated for various acceptor concentrations in Fig. 7. It can be clearly observed that  $V_{OC}$  increases from 0.80 V to 0.86 V as the SnS-P<sup>+</sup> concentration increases from  $3 \times 10^{18}$  cm<sup>-3</sup> to  $3 \times 10^{19}$  cm<sup>-3</sup>. We also observe that there is a slight increase in  $J_{SC}$ . For this reason, we have chosen two acceptor density values of the SnS-P<sup>+</sup> layer as a function of the electric field in Fig. 8. We can observe for the two density values that when we increase the carrier concentration to  $3 \times 10^{19}$  cm<sup>-3</sup>, the electric field increases near the rear interface Mo/SnS. As a result, the quantum efficiency with respect to wavelength for various acceptor concentrations of the BSF (SnS) layer is provided in Fig. 9. It can be seen that the QE for

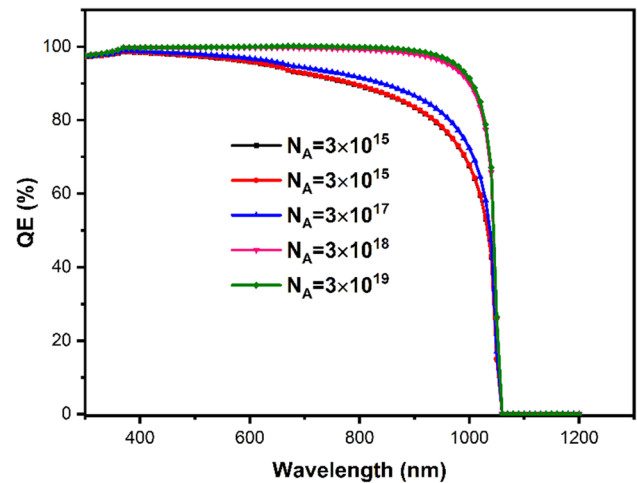


**Fig. 9** Quantum efficiency of CIGS-based solar cells with BSF (SnS) for different acceptor density values.

a higher  $N_{A(\text{SnS})}$  value is superior for long wavelengths. Increased acceptor density improves the electron transfer mechanism in a photovoltaic cell.<sup>5,34</sup> The optimum CIGS solar cell performance was acquired at BSF (SnS) carrier concentration and thickness of  $3 \times 10^{19}$  cm<sup>-3</sup> and 40 nm, respectively.

### Effect of BSF (SnS) Layer Band Gap on CIGS Cell Performance

The following step is to optimize the SnS BSF band gap. Figure 10 depicts the variation in  $V_{OC}$ ,  $J_{SC}$ , FF, and PCE parameters versus the energy band gap for a BSF (SnS) thickness of 40 nm and  $N_{A(\text{SnS})} = 3 \times 10^{19}$  cm<sup>-3</sup>. We can see that the cell performance is lower for a small gap ( $E_g = 1.1$  eV) and then improves as the gap energy grows until it reaches a short-circuit current equal to 39.92 mA/cm<sup>2</sup> and a maximum efficiency of 29.79% for  $E_g = 1.32$  eV, after which the PCE is almost constant. The  $V_{OC}$  increases until obtaining a maximum voltage of 0.87 V for a gap energy of 1.35 eV, but the case is different for FF which increases to FF = 86.12% for  $E_g = 1.3$  eV and then decreases to reach 84.34% for  $E_g = 1.35$  eV. The electric field generated at the back SnS and Mo contact for various gaps from 1.1 eV to 1.32 eV is depicted in Fig. 11. We can notice that the electric field rises as the BSF (SnS) material band gap is 1.32 eV for PCE = 29.79%. The electric field is higher and generates more energy efficiency when the band gap of the BSF layer is large. However, beyond 1.3 eV, the fill factor decreases.<sup>29,36</sup> This reduction in FF is influenced by the barrier height formed for charge carrier holes in the valence band diagram. According to Eq. 5, the fill factor is expressed as the ratio of theoretical power  $P_{th} = J_{SC} \times V_{OC}$  to the maximum power available

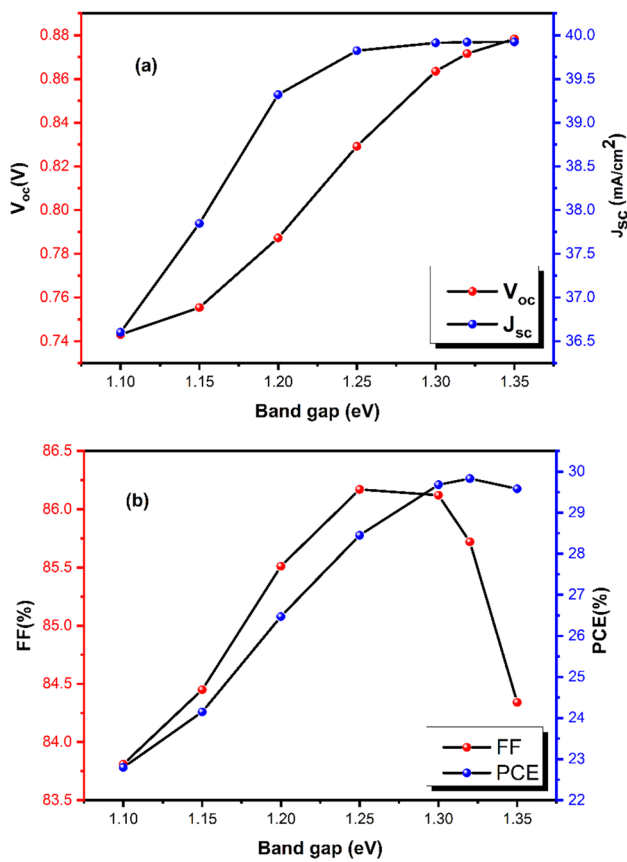


Fig. 10 The variation of device performance with respect to the band gap energy of the BSF layer (SnS). (a)  $V_{OC}$  and  $J_{SC}$ . (b) FF and PCE.

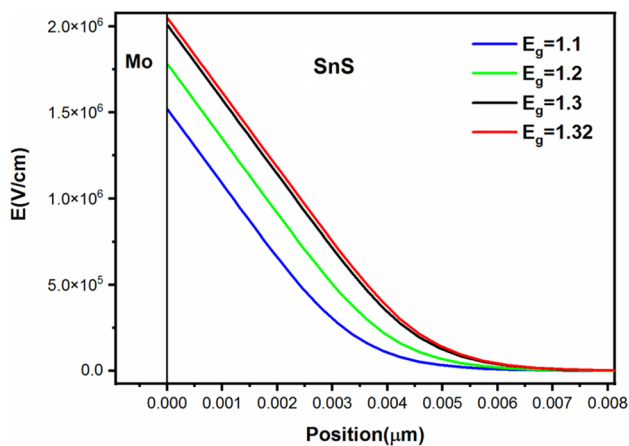


Fig. 11 Electric field for a CIGS solar cell with different BSF (SnS) layer gap energy values.

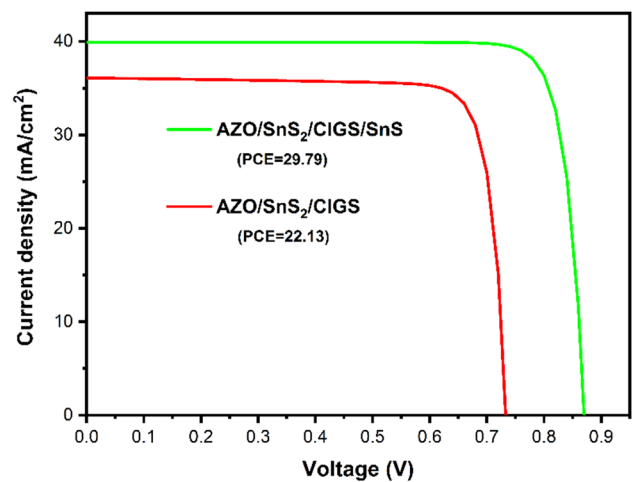


Fig. 12  $J$ - $V$  characteristic of a CIGS solar cell with and without BSF (SnS) layer.

$P_{max} = J_{max} \times V_{max}$ ; when the FF decreases, the  $V_{OC}$  and  $J_{SC}$  increase. In this analysis, we chose 1.32 eV as the optimal value for the band gap of the BSF layer.

### The Characteristics of the Solar Device with and without BSF

The impact of incorporating the SnS-P<sup>+</sup> layer on the current-voltage characteristics is depicted in Fig. 12. The introduction of a SnS-P<sup>+</sup> layer on the rear face of the Mo/SnS/CIGS/SnS<sub>2</sub>/AZO solar cell design leads to a substantial enhancement of the PV performance of the examined cell. With the added BSF layer (SnS), the open-circuit voltage went up from 0.63 V without to 0.87 V with SnS-P<sup>+</sup>. The correct alignment of the BSF band in the suggested structure will result in a more significant embedded potential due to the larger band offset, which increases the open-circuit voltage.<sup>37</sup>

In the CIGS solar cell, the fill factor increased from 83.51% for the solar cell without SnS-P<sup>+</sup> to 85.68% for the solar cell with SnS-P<sup>+</sup> layer. This increase of around 2.17% can be explained by an increase in the most significant power  $P_m$  created by the Mo/SnS/CIGS/SnS<sub>2</sub>/AZO structure PV cell. This increase in maximum external power is the result of the electric field created on the rear face of the cell, as shown in Fig. 13, which allows the reduction of the recombination rate near the molybdenum back contact as shown in Fig. 14. The presence of an electric field near the ohmic contact at the back side allows the minority charge

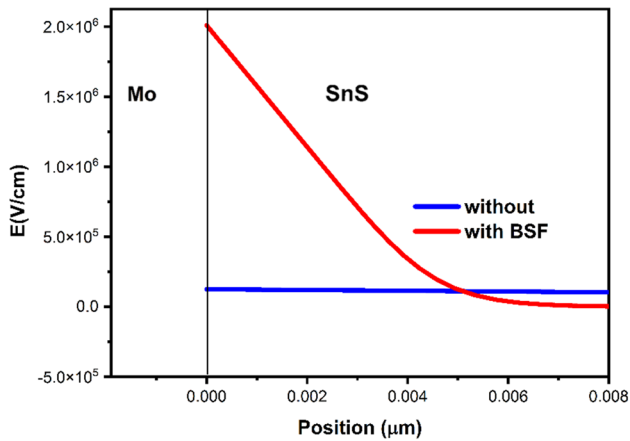


**Fig. 13** Electric field for a CIGS solar cell with and without BSF (SnS) layer.

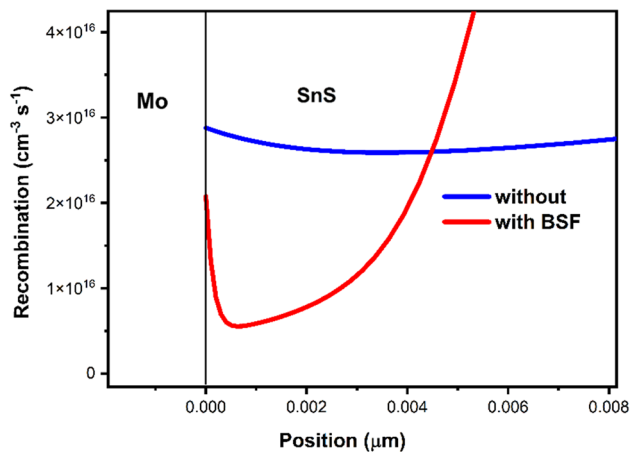


**Fig. 14** Recombination rate for a CIGS solar cell with and without BSF (SnS) layer.

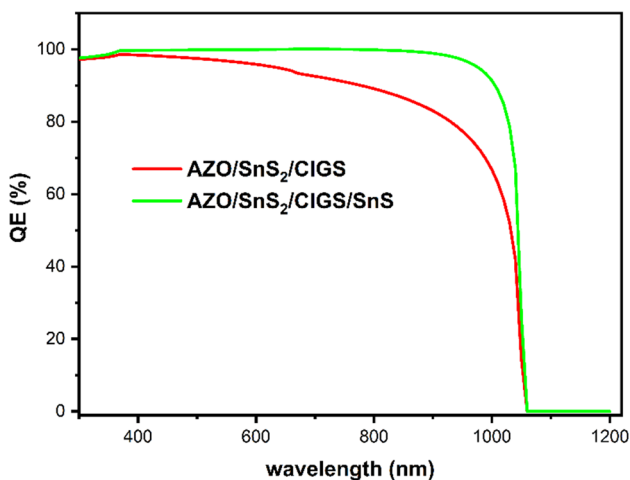


**Fig. 15** Quantum efficiency of a CIGS solar cell with and without BSF (SnS) layer.

**Table II** The simulation results with and without SnS-P<sup>+</sup> layer.

Type of CIGS cell	$V_{OC}$ (V)	$J_{SC}$ (mA/cm <sup>2</sup> )	FF (%)	PCE (%)
Mo/CIGS/SnS <sub>2</sub> /AZO	0.73	36.09	83.51	22.13
Mo/SnS/CIGS/SnS <sub>2</sub> /AZO	0.87	39.92	85.68	29.79

carriers to be forced toward the area of the depletion region for improved collection,<sup>38</sup> which is obviously confirmed by the QE diagrams as seen in Fig. 15. These modifications led to a substantial increase in the performance efficiency of solar energy conversion of the CIGS cell, increasing from 22.13% for a cell without SnS-P<sup>+</sup> to 29.79% for the cell with the SnS-P<sup>+</sup> layer inserted, given the best collection of charge carriers and the excellent stability by the existence of this back surface layer. Further, we have summarized these results in Table II.

In Fig. 15, the CIGS solar cell has high absorption that achieves a quantum efficiency of about 100%, which results in a strong electron–hole pair creation with little reflection at the front surface. For wavelengths shorter than 400 nm, the observed losses are clearly caused by the reflection on the front side. For lengths > 1100 nm, a strong decrease in quantum efficiency is seen as a result of the transmission of the low-energy photons that cannot be harvested in the solar cell. Typically, the medium-energy photons are captured at the back contact region, and the carrier charges created by this photon energy lead to a slight increase in the energy efficiency of the device due to their strong possibility for recombination.<sup>32</sup>

## The Effect of Temperature on the Cell Performance

The performance of photovoltaic devices is significantly affected by the operating temperature, the optimum value of which is 300 K for the studied CIGS solar cell. In this work, we increased the temperature from 300 K to 400 K. The results of the device behaviour with respect to the temperature are illustrated in Fig. 16. Because of an increase in light absorption,  $J_{SC}$  tends to rise slightly or exhibits behaviour irrespective of temperature due to an increase in photon absorption.<sup>39,40</sup> As the temperature rises, electrons receive more energy, and they are extremely likely to recombine with holes before arriving at the depletion region. Therefore, the temperature significantly impacts the hole and electron mobility, which negatively affects the FF, PCE, and  $V_{OC}$ .<sup>18</sup>

$$V_{OC} = \frac{nkT}{q} \left( \log \frac{J_{SC}}{J_0} + 1 \right) \quad (6)$$



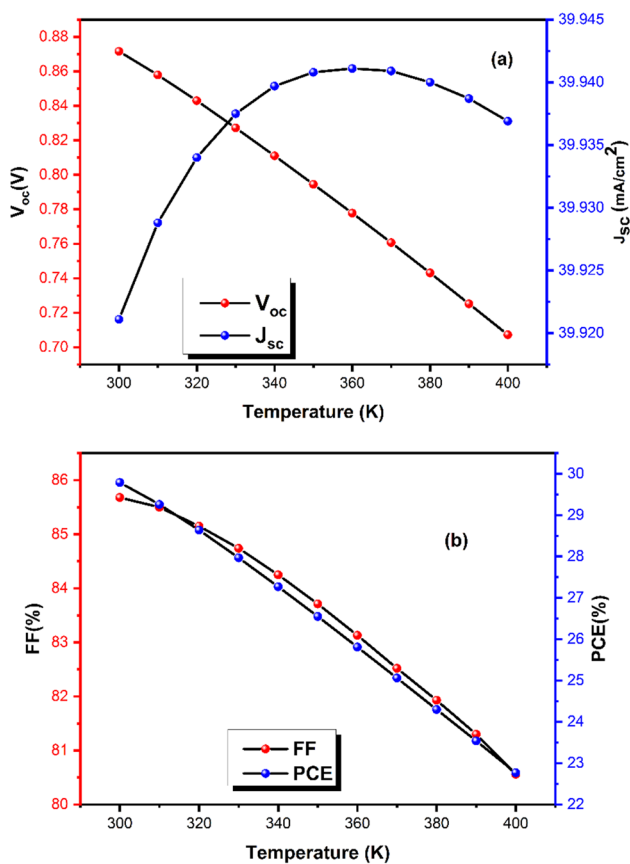


**Fig. 16** Temperature effect on the photovoltaic parameters. (a)  $V_{OC}$  and  $J_{SC}$  variation. (b) FF and PCE variation.

Equation 6 can be used to explain the relationship between  $V_{OC}$  and  $J_{SC}$ , where  $T$  is the working temperature,  $K$  is the Boltzmann constant,  $q$  is the electronic charge,  $n$  is the ideality factor, and  $J_0$  the reverse saturating current. When the temperature rises, it causes an exponential increase in the reverse saturation current, which lowers the  $V_{OC}$ . Again, more carriers are produced at high heat, resulting in an increase of  $J_{SC}$ . However, due to the rise in phonon density, the occurrence of phonon scattering could prevail at this high temperature. Because of this scattering effect, the average free path of the carriers becomes shorter, resulting in more electron–hole recombination and a reduction in  $V_{OC}$ . Furthermore, the scattering effect provides resistance to the mobility of charge transfer, and as a result, FF drops significantly due to this resistance. The lowering in device efficiency is caused due to the decrease in fill factor and open-circuit voltage.<sup>22</sup>

## Comparative Research

The benefit of adding an ultra-thin BSF (SnS) layer in CIGS-based TFSCs has been investigated in this research employing SnS<sub>2</sub> as a buffer layer. This cell is characterized by an efficiency of 22.13% with a thin absorber layer of 1  $\mu\text{m}$  and a buffer layer of 0.05  $\mu\text{m}$  without including the BSF layer. However, the introduction of the BSF layer improves the efficiency significantly. A wide range of materials, including Si, SiO<sub>2</sub>, Al<sub>2</sub>O<sub>3</sub>, Cu<sub>2</sub>O, CIS, MoSe<sub>2</sub>, PbS, and SnS were used as the BSF layer by other researchers, and their results are presented in Table III to compare the energy efficiency values with this work. Although the SnS material has already been studied as a BSF layer in several works, it has not yet achieved higher efficiency than 29.79%.

## Conclusion

In this research work, the photovoltaic cell structure used for the numerical simulation is Mo/SnS/CIGS/SnS<sub>2</sub>/AZO, which has been optimized by SCAPS-1D software. The present paper aims to study the characteristics of CIGS-based solar devices for which we have optimized parameters such as the thickness, doping density, and band gap of the back surface field layer SnS-P<sup>+</sup> to improve energy conversion efficiency. We have also investigated the effect of the working temperature on the performance of the studied cell. The CIGS cell without the BSF (SnS) layer shows a PCE of 22.13%, with FF of 83.51,  $J_{SC}$  of 36.09 mA/cm<sup>2</sup> and  $V_{OC}$  of 0.7340 V, for an absorber layer with 1  $\mu\text{m}$  thickness. Thus, after introducing a 40 nm-thick BSF layer, optimal values of  $3 \times 10^{19} \text{ cm}^{-3}$  and 1.32 eV can be set for doping concentration and band gap, respectively. Because of the strong electric field generated by the insertion of the BSF layer, the power conversion efficiency obtained is 29.79%, fill factor of 85.68%, short-circuit current density of 39.92 mA/cm<sup>2</sup> and an open-circuit voltage of 0.87 V for an active layer thickness equal to 1  $\mu\text{m}$ . The obtained results are interesting because they encourage the use of clean, inexpensive and abundant materials for obtaining high-efficiency thin-film solar cells: the SnS<sub>2</sub> material as a buffer layer replacing conventional CdS which should be avoided due to its toxicity, and the SnS material which can be elaborated by a simple, convenient, and inexpensive chemical bath deposition process as a BSF layer. The characteristics of the CIGS solar cell suggested in this study have led to more effective

**Table III** Comparison of characteristics with several other works studied

Work type	Absorber layer	Buffer layer	BSF layer	PCE (%) with BSF	References
Experimental	CIGSe	CdS	MoS <sub>2</sub>	8.73	41
Experimental	c-Si(n)	c-Si(p)	ZnS	11.02	42
Experimental	CZT(S,Se)	CdS	MoS <sub>2</sub>	12.30	27
Experimental	CIGS	CdS	SiO <sub>2</sub>	15.6	43
Simulation	CZTS	AZTS	CZTS	5.05	10
Simulation	CZT(S,Se)	SnS <sub>2</sub>	MoS <sub>2</sub>	12.57	27
Simulation	CZTS	SnS <sub>2</sub>	MoS <sub>2</sub>	12.73	17
Simulation	CIGS	CdS	Al <sub>2</sub> O <sub>3</sub>	13.08	23
Simulation	Sb <sub>2</sub> Se <sub>3</sub>	Zn <sub>0.93</sub> Mg <sub>0.07</sub> O/ZnO <sub>0.4</sub> S <sub>0.6</sub>	MoSe <sub>2</sub>	15.46	44
Simulation	CdTe	CdS	MoO <sub>3</sub>	27.90	45
Simulation	CdTe	CdS	V <sub>2</sub> O <sub>5</sub>	23.50	46
Simulation	CdTe	CdS	SnS	17.40	38
Simulation	CIGS	ZnMgO/ Zn(O,S)	CuS	17.67	47
Simulation	Sb <sub>2</sub> Se <sub>3</sub>	CdS	SnS	17.75	1
Simulation	CZTS	SnS <sub>2</sub>	MoS <sub>2</sub>	18.94	18
Simulation	CZTS	In <sub>2</sub> S <sub>3</sub>	MoS <sub>2</sub>	19.03	18
Simulation	CZTSSe	CdS	Zn <sub>3</sub> P <sub>2</sub>	19.70	48
Simulation	CIGS	CdS	Si	21.3	49
Simulation	CZTS <sub>0.8</sub> Se <sub>0.2</sub>	CdS	a-Si:H	22.45	50
Simulation	SnSe	CdS	NiO	22.69	51
Simulation	CIGS	CdS	PbS	24.22	22
Simulation	CIGS	ZnMgO/ Zn(O,S)	CuSCN	24.4	47
Simulation	CIGS	CdS	CIS	25.05	52
Simulation	CIGS	CdS	Si	26	1
Simulation	CIGS	ZnS	MoSe <sub>2</sub>	26.30	53
Simulation	CIGS	ZnMgO/ Zn(O,S)	Cu <sub>2</sub> O	27.3	47
Simulation	CIGS	SnS <sub>2</sub>	SnS	29.79	This research

and efficient results in terms of energy conversion. We expect that this research will contribute to the improved performance and cost-effectiveness of CIGS solar cells in the near future.

**Acknowledgments** The authors would like to express their gratitude to Marc Burgelman and his team from the Department of Electronics and Information Systems (ELIS), University of Ghent, Belgium, for providing unrestricted access to SCAPS software version 3.3.07 for academic use.

**Conflict of interest** The authors declare that they have no known competing financial interests or personal relationships that would have appeared to have influenced the research reported in this work.

## References

- R.N. Mohottige and S.P.K. Vithanage, Numerical simulation of a new device architecture for CIGS-based thin-film solar cells using 1D-SCAPS simulator. *J. Photochem. Photobiol. A: Chem.* 407, 113079 (2021).
- A. Romeo and E. Artagiani, CdTe-based thin film solar cells: past, present and future. *Energies* 14, 1684 (2021).
- M. Powalla, S. Paetel, E. Ahlswede, R. Wuerz, C.D. Wessendorf, and T.M. Friedlmeier, Thin-film solar cells exceeding 22% solar cell efficiency: an overview on CdTe-, Cu (In, Ga) Se<sub>2</sub>-, and perovskite-based materials. *Appl. Phys. Rev.* 5, 041602 (2018).
- A. Hosen and S.R. Al Ahmed, Performance analysis of SnS solar cell with a hole transport layer based on experimentally extracted device parameters. *J. Alloy Compd.* 909, 164823 (2022).
- A.K. Patel, P.K. Rao, R. Mishra, and S.K. Soni, Numerical study of a high-performance thin film CIGS solar cell with a-Si and MoTe<sub>2</sub> hole transport layer. *Optik* 243, 167498 (2021).
- F.-W. Liu, T.-M. Cheng, Y.-J. Chen, K.-C. Yueh, S.-Y. Tang, K. Wang, and C.-L. Wu, High-yield recycling and recovery of copper, indium, and gallium from waste copper indium gallium selenide thin-film solar panels. *Sol. Energy Mater. Sol. Cells* 241, 111691 (2022).
- A.J.N. Oliveira, J.P. Teixeira, D. Ramos, P.A. Fernandes, and P.M.P. Salomé, Exploiting the optical limits of thin-film solar cells: a review on light management strategies in Cu (In, Ga) Se<sub>2</sub>. *Adv. Photonics Res.* 3, 2100190 (2022).
- J. Zikulnig, W. Mühleisen, P.J. Bolt, M. Simor, and M. De Biasio, Photoluminescence imaging for the in-line quality control of thin-film solar cells. *Solar* 2, 1 (2022).
- A. Debot, V.B. Chu, D. Adeleye, J. Guillot, D. Arl, M. Melchiorre, and P.J. Dale, Inkjet-printed indium sulfide buffer layer for Cu (In,

- Ga)(S, Se)<sub>2</sub> thin film solar cells. *Thin Solid Films* 745, 139096 (2022).
10. M. Jamil, M. Amami, A. Ali, K. Mahmood, and N. Amin, Numerical modeling of AZTS as buffer layer in CZTS solar cells with back surface field for the improvement of cell performance. *Sol. Energy* 231, 41 (2022).
  11. S. Tobbeche, S. Kalache, M. Elbar, M.N. Kateb, and M.R. Serdouk, Improvement of the CIGS solar cell performance: structure based on a ZnS buffer layer. *Opt. Quantum Electron.* 51, 1 (2019).
  12. O.A. Jaramillo-Quintero, A. Baron-Jaimes, R.A. Miranda-Gamboa, and M.E. Rincon, Cadmium-free ZnS interfacial layer for hydrothermally processed Sb<sub>2</sub>S<sub>3</sub> solar cells. *Sol. Energy* 224, 697 (2021).
  13. F. Takagi, Y. Kageshima, K. Teshima, K. Domen, and H. Nishikiori, Enhanced photoelectrochemical performance from particulate ZnSe: Cu(In, Ga)Se<sub>2</sub> photocathodes during solar hydrogen production via particle size control. *Sustain. Energy Fuels* 5, 412 (2021).
  14. M.R. Hasan, M.S. Irtiza, and M.J. Hasan, Application scope of ZnSe-In<sub>2</sub>S<sub>2</sub> as a dual buffer layer as a substitute of CdS buffer layer in CIGS based solar cell. *Int. J. Innov. Sci. Res. Technol.* 5, 1125 (2020).
  15. S. Gedi, S. Alhammadi, J. Noh, V.R.M. Reddy, H. Park, A.M. Rabie, J.-J. Shim, D. Kang, and W.K. Kim, SnS<sub>2</sub> nanoparticles and thin film for application as an adsorbent and photovoltaic buffer. *Nanomaterials* 12, 282 (2022).
  16. A. Degrauw, R. Armstrong, A.A. Rahman, J. Ogle, and L. Whitaker-Brooks, Catalytic growth of vertically aligned SnS/SnS<sub>2</sub> p-n heterojunctions. *Mater. Res. Express* 4, 094002 (2017).
  17. F. Belarbi, W. Rahal, D. Rached, and M. Adnane, A comparative study of different buffer layers for CZTS solar cell using Scaps-1D simulation program. *Optik* 216, 164743 (2020).
  18. S. Tripathi, B. Kumar, and D.K. Dwivedi, Numerical simulation of non-toxic In<sub>2</sub>S<sub>3</sub>/SnS<sub>2</sub> buffer layer to enhance CZTS solar cells efficiency by optimizing device parameters. *Optik* 227, 166087 (2021).
  19. S. Ullah, A. Bouich, H. Ullah, B. Mari, and M. Mollar, Comparative study of binary cadmium sulfide (CdS) and tin disulfide (SnS<sub>2</sub>) thin buffer layers. *Sol. Energy* 208, 637 (2020).
  20. N.E.I. Boukortt and S. Patanè, Single junction-based thin-film CIGS solar cells optimization with efficiencies approaching 2.45%. *Optik* 218, 165240 (2020).
  21. N. Mufti, T. Amrillah, A. Taufiq, M. Diantoro, and H. Nur, Review of CIGS-based solar cells manufacturing by structural engineering. *Sol. Energy* 207, 1146 (2020).
  22. B. Barman and P.K. Kalita, Influence of back surface field layer on enhancing the efficiency of CIGS solar cell. *Sol. Energy* 216, 329 (2021).
  23. N.E.I. Boukortt, S. Patanè, M. Adouane, and R. AlHammedi, Numerical optimization of ultrathin CIGS solar cells with rear surface passivation. *Sol. Energy* 220, 590 (2021).
  24. M.S. Rana, M.M. Islam, and M. Julkarnain, Enhancement in efficiency of CZTS solar cell by using CZTSe BSF layer. *Sol. Energy* 226, 272 (2021).
  25. W. Liu, H. Li, B. Qiao, S. Zhao, Z. Xu, and D. Song, Highly efficient CIGS solar cells based on a new CIGS bandgap gradient design characterized by numerical simulation. *Sol. Energy* 233, 337 (2022).
  26. M.K. Sobayel, M.S. Chowdhury, T. Hossain, H.I. Alkhamash, S. Islam, M. Shahiduzzaman, and K. Md Akhtaruzzaman, Efficiency enhancement of CIGS solar cell by cubic silicon carbide as prospective buffer layer. *Sol. Energy* 224, 271 (2021).
  27. M. Haghghi, M. Minbashi, N. Taghavinia, D.-H. Kim, S.M. Mahdavi, and A.A. Kordbacheh, A modeling study on utilizing SnS<sub>2</sub> as the buffer layer of CZT(S, Se) solar cells. *Sol. Energy* 167, 165 (2018).
  28. T. Pansuriya, R. Malani, and V. Kheraj, Investigations on the effect of buffer layer on CMTS based thin film solar cell using SCAPS 1-D. *Opt. Mater.* 126, 112150 (2022).
  29. H. Aissani, A. Helmaoui, and H. Moughli, Numerical modeling of graded band-gap cigs solar cell for high efficiency. *Int. J. Appl. Eng. Res.* 12, 227 (2017).
  30. K.R. Ngoy, A.K. Singh, T.-C. Jen, and A.M. Ali, Numerical analysis of thin film Cu<sub>2</sub>InGaSe<sub>4</sub> solar cells design. *Sol. Energy* 225, 53 (2021).
  31. T. AlZoubi, A. Moghrabi, M. Moustafa, and S. Yasin, Efficiency boost of CZTS solar cells based on double-absorber architecture: Device modeling and analysis. *Sol. Energy* 225, 44 (2021).
  32. V.C. Karade, J.S. Jang, D. Kumbhar, M. Rao, P.S. Pawar, S. Kim, K.S. Gour et al., Combating open circuit voltage loss in Sb<sub>2</sub>Se<sub>3</sub> solar cell with an application of SnS as a back surface field layer. *Sol. Energy* 233, 435 (2022).
  33. B.C. Mohanty, Improving performance of Cu<sub>2</sub>ZnSnS<sub>4</sub> solar cell via back contact interface engineering. *Sol. Energy* 230, 986 (2021).
  34. E. Oublal, M. Sahal, and A.A. Abdelkadir, New theoretical analysis of a novel hetero-junction SnS/CdS solar cell with homo-junction P-P<sup>+</sup> in the rear face-numerical approach. *Curr. Appl. Phys.* 39, 230 (2022).
  35. K. Ali, and Z. Ali, Analytical study of electrical performance of SiGe-based n+-p-p<sup>+</sup> solar cells with BaSi<sub>2</sub> BSF structure. *Sol. Energy* 225, 91 (2021).
  36. A. Lafuente-Sampietro, K. Yoshida, S. Wang, S. Ishizuka, H. Shibata, N. Sano, K. Akimoto, and T. Sakurai, Effect of the double grading on the internal electric field and on the carrier collection in CIGS solar cells. *Sol. Energy Mater. Sol. Cells* 223, 110948 (2021).
  37. M. Al-Hattab, M. Khenfouch, O. Bajjou, Y. Chrafi, and K. Rahmani, Numerical simulation of a new heterostructure CIGS/GaSe solar cell system using SCAPS-1D software. *Sol. Energy* 227, 13 (2021).
  38. S. Benabbas, Z. Rouabah, N. Bouarissa, and N. Chelali, The role of back surface field SnS layer in improvement of efficiency of CdTe thin film solar cells. *Optik* 127(15), 6210 (2016).
  39. P. Singh, and N.M. Ravindra, Temperature dependence of solar cell performance-an analysis. *Sol. Energy Mater. Sol. Cells* 101, 36 (2012).
  40. M.A. Green, General temperature dependence of solar cell performance and implications for device modelling. *Prog. Photovolt. Res. Appl.* 11, 333 (2003).
  41. S.-T. Kim, V. Bhatt, Y.-C. Kim, H.-J. Jeong, J.-H. Yun, and J.-H. Jang, Formation of MoSe<sub>2</sub> layer and Ga grading in flexible Cu (In, Ga) Se<sub>2</sub> solar cell via Na diffusion. *J. Alloy. Compd.* 899, 163301 (2022).
  42. X. Yang, B. Chen, J. Chen, Y. Zhang, W. Liu, and Y. Sun, ZnS thin film functionalized as back surface field in Si solar cells. *Mater. Sci. Semicond. Process.* 74, 309 (2018).
  43. F. Ghamsari-Yazdel, and A. Fattah, Performance enhancement of CIGS solar cells using ITO as buffer layer. *Micro Nanostruct.* 168, 207289 (2022).
  44. I. Gharibshahian, A.A. Orouji, and S. Sharbati, Towards high efficiency Cd-Free Sb<sub>2</sub>Se<sub>3</sub> solar cells by the band alignment optimization. *Sol. Energy Mater. Sol. Cells* 212, 110581 (2020).
  45. Ç. Çetinkaya, Efficient and high-bifacial CdTe-based solar cell enabled by functional designed dielectric/metal/dielectric transparent top contact via light management engineering. *Opt. Mater.* 133, 113003 (2022).
  46. A. Kuddus, M.F. Rahman, S. Ahmmed, J. Hossain, and A.B.M. Ismail, Role of facile synthesized V<sub>2</sub>O<sub>5</sub> as hole transport layer for CdS/CdTe heterojunction solar cell: validation of simulation using experimental data. *Superlattices Microstruct.* 132, 106168 (2019).

47. I. Gharibshahian, A.A. Orouji, and S. Sharbati, Effectiveness of band discontinuities between CIGS absorber and copper-based hole transport layer in limiting recombination at the back contact. *Mater. Today Commun.* 33, 104220 (2022).
48. P.S. Babu, P.K. Singh, A.K. Thakur, and D.K. Dwivedi, Optimization of photovoltaic solar cell performance via the earth abundant  $Zn_3P_2$  back surface field. *Optik* 229, 166235 (2021).
49. H. Heriche, Z. Rouabah, and N. Bouarissa, New ultra thin CIGS structure solar cells using SCAPS simulation program. *Int. J. Hydrogen Energy* 42, 9524 (2017).
50. N. Kumari, and S. Ingole, Enhancement of CZTS photovoltaic device performance with silicon at back-contact: a study using SCAPS-1D. *Sol. Energy* 236, 301 (2022).
51. R.K. Yadav, P.S. Pawar, R. Nandi, K.E. Neerugatti, Y.T. Kim, J.Y. Cho, and J. Heo, A qualitative study of SnSe thin film solar cells using SCAPS 1D and comparison with experimental results: a pathway towards 22.69% efficiency. *Sol. Energy Mater. Solar Cells* 244, 111835 (2022).
52. N.E.I. Boukortt, S. Patanè, and Y.M. Abdulraheem, Numerical investigation of CIGS thin-film solar cells. *Sol. Energy* 204, 440 (2020).
53. T.N. Fridolin, D.K.G. Maurel, G.W. Ejuh, T.T. Benedicte, and J.M. Ndjaka, Highlighting some layers properties in performances optimization of CIGSe based solar cells case of Cu (In, Ga) Se–ZnS. *J King Saud Univ.-Sci.* 31(4), 1404 (2019).

**Publisher's Note** Springer Nature remains neutral with regard to jurisdictional claims in published maps and institutional affiliations.

Springer Nature or its licensor (e.g. a society or other partner) holds exclusive rights to this article under a publishing agreement with the author(s) or other rightsholder(s); author self-archiving of the accepted manuscript version of this article is solely governed by the terms of such publishing agreement and applicable law.